Spherical and deformed high-spin states in ^{38}Ar

D. Rudolph,[1] A. Poves,[2] C. Baktash,[3] R. A. E. Austin,[4] J. Eberth,[5] D. Haslip,[4,*] D. R. LaFosse,[6,†] M. Lipoglavšek,[3,‡] S. D. Paul,[3,§] D. G. Sarantites,[6] C. E. Svensson,[4,‖] H. G. Thomas,[5] J. C. Waddington,[4] W. Weintraub,[7] and J. N. Wilson[4,¶]
[1]*Department of Physics, Lund University, S-22100 Lund, Sweden*
[2]*Departamento de Física Teórica, Universidad Autónoma de Madrid, E-28049 Madrid, Spain*
[3]*Physics Division, Oak Ridge National Laboratory, Oak Ridge, Tennessee 37831*
[4]*Department of Physics and Astronomy, McMaster University, Hamilton, Ontario, Canada L8S 4M1*
[5]*Institut für Kernphysik, Universität zu Köln, D-50937 Köln, Germany*
[6]*Chemistry Department, Washington University, St. Louis, Missouri 63130*
[7]*Department of Physics, University of Tennessee, Knoxville, Tennessee 37996*
(Received 24 August 2001; published 13 February 2002)

Excited states in ^{38}Ar have been investigated by means of the heavy-ion fusion-evaporation reaction ^{28}Si $+^{16}$O. The level scheme reveals a subtle interplay between spherical, deformed, and superdeformed shapes. Large-scale shell-model calculations in the *sd-fp* space are invoked to study the microscopic aspects of deformation and shape changes.

DOI: 10.1103/PhysRevC.65.034305 PACS number(s): 23.20.Lv, 21.60.Cs, 27.30.+t

I. INTRODUCTION

Experimental studies of doubly magic nuclei and nearby neighbors provide important benchmarks to test nuclear models. At high excitation energy or angular momentum single-particle and collective modes of excitation may compete in these systems. This may allow for a comparison of different microscopic theoretical treatments and can lead to an understanding of collective motion in terms of the spherical shell model. This has been demonstrated recently in the case of ^{56}Ni, where rotational bands have been identified. These bands are based on four-particle four-hole ($4p$-$4h$) excitations across the $N,Z=28$ shell gap [1].

Similarly, in ^{40}Ca the first excited 0_2^+ state at 3353 keV has been interpreted for a long time as $4p$-$4h$ excitation across the $N,Z=20$ shell gap [2]. This state forms the bandhead of a prolate-deformed rotational band. Later on this interpretation was confirmed by measurements of large $B(E2;2^+\rightarrow 0_2^+)$ and $B(E2;4^+\rightarrow 2^+)$ transition strengths [3,4]. While the location of the yrast 6^+ state indicates the succession of a reasonably smooth $J(J+1)$ behavior of the sequence, the yrast 8^+ forms an early example of band termination [5]. The leading components of the wave function of the 8^+ state in ^{40}Ca are $2p$-$2h$ excitations. Recently, a candidate for a superdeformed $8p$-$8h$ structure in ^{40}Ca has been identified, which is built on the 0_3^+ state [6]. In the neighboring nucleus ^{36}Ar, which has one α particle fewer than ^{40}Ca, the $4p$-$8h$ band has been extended up to spin $I=16$ [7].

The present study aims at the identification of deformed multiparticle multihole high-spin states in ^{38}Ar. They are expected to compete with near-spherical ''terminating'' states of lower seniority. Excited states in ^{38}Ar have been studied extensively with light-ion-induced reactions (see compilation by Endt [4]), while the most recent high-spin result dates back to the late 1970s [8]. Section II describes the experimental procedures and results. It is followed by Sec. III, which presents an interpretation of the new data in the framework of large-scale shell-model calculations.

II. EXPERIMENT

The experiment was performed at the 88-Inch Cyclotron at Lawrence Berkeley National Laboratory. The heavy-ion fusion evaporation reaction ^{28}Si$+^{16}$O was used at 125 MeV beam energy. High-spin states in ^{38}Ar were populated via $1\alpha 2p$ evaporation from the compound nucleus ^{44}Ti. The GAMMASPHERE Ge-detector array [9] was coupled to the 4π charged-particle detector array MICROBALL [10] and 15 liquid scintillator neutron detectors to allow for a proper selection of the various reaction channels. The neutron detectors replaced the Ge detectors in the three most forward rings of GAMMASPHERE. The target was a ~ 0.5 mg/cm^2 thin enriched ^{40}Ca foil which suffered from considerable oxidation. Since the natural abundance of ^{16}O is 99.8%, the only measurable reaction cross section with oxygen can arise from this isotope. Reactions of the ^{28}Si beam with either ^{40}Ca or ^{16}O can be clearly discriminated because of (i) the different recoil velocities ($v=3.4\%\ c$ and $v=5.7\%\ c$, respectively) and (ii) the different total energy E_{tot} and average maximum spin of the compound nucleus. The γ-ray multiplicity K and total energy H could be measured since the hevimet absorbers in front of the anti-Compton shields of the Ge detectors were removed [11]. Using the energy E_{part} deposited in MICROBALL by the evaporated charged particles, the reaction of interest can be selected with a proper gate in a two-dimensional plot of K vs $E_{tot}=H+E_{part}$ [12].

The data were sorted off-line into a number of reaction-channel-selected two- and three-dimensional $\gamma\gamma$ matrices and $\gamma\gamma\gamma$ cubes. The RADWARE data analysis software [13] and the spectrum-analysis code TV [14] were used to inves-

*Present address: DRE Ottawa, Ontario, Canada.
†Present address: SUNY Stony Brook, NY 11794.
‡Present address: J. Stefan Institute, Ljubljana 1000, Slovenia.
§Present address: TIFR, Bombay 400 005, India.
‖Present address: University of Guelph, Guelph, Ontario, Canada.
¶Present address: NBI, DK-2100 Copenhagen, Denmark.

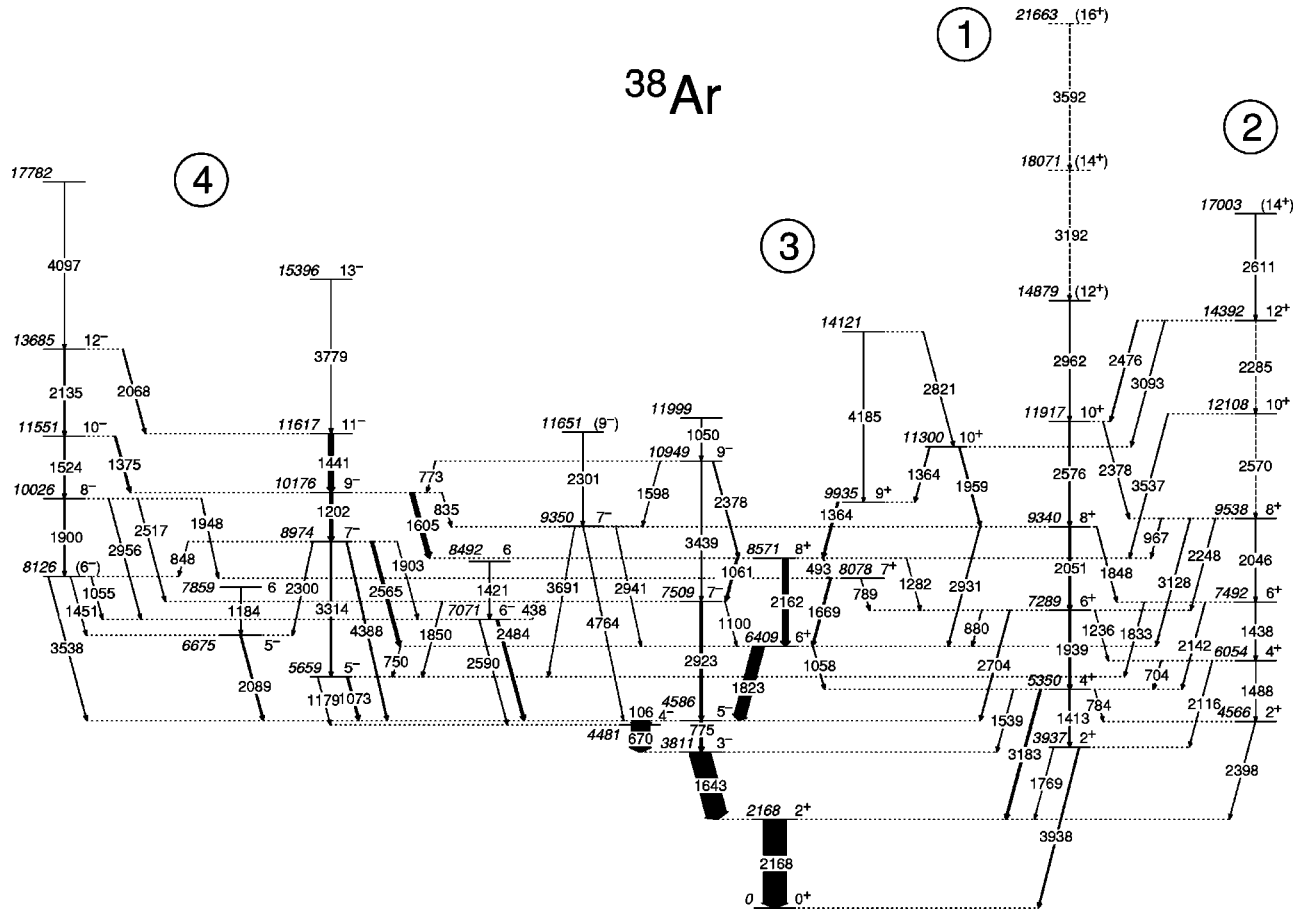

FIG. 1. Proposed partial experimental level scheme of ^{38}Ar. The energy labels are given in keV. The widths of the arrows are proportional to the relative intensities of the γ rays. Tentative transitions and levels are dashed.

tigate γ-ray coincidences and intensities.

E_γ-E_γ angular correlations between γ rays detected in the backward section ($\overline{\Theta}=150°$) and the central section ($\overline{\Theta}=97°$) were investigated by means of directional correlations of oriented states (DCO ratios) [15]

$$R_{DCO}(\gamma_1,\gamma_2)=\frac{I(\gamma_1 \text{ at } 150°;\ \text{gated with } \gamma_2 \text{ at } 97°)}{I(\gamma_1 \text{ at } 97°;\ \text{gated with } \gamma_2 \text{ at } 150°)}. \quad (1)$$

The R_{DCO} values were corrected for the slightly different detection efficiencies in the different Ge-detector rings. Known stretched $E2$ transitions [8] were used for gating, such that $R_{DCO}=1.0$ is expected for observed stretched quadrupole transitions and $R_{DCO}\sim 0.6$ for stretched pure dipoles. Nonstretched $\Delta I=0$ transitions have typically $R_{DCO}\sim 1.0$, which also depends on the multipole mixing ratio.

The level scheme of ^{38}Ar from the present analysis is shown in Fig. 1 and summarized in Table I. It considerably extends the previously reported high-spin excitation scheme by Aarts *et al.* [8]. Except for one case, previous spin assignments of states were confirmed, and earlier parity assignments [4,8] were adopted.

Figure 2 provides a number of γ-ray spectra, which focus on newly identified sequences in the level scheme of ^{38}Ar. All spectra are in coincidence with one evaporated α particle and two protons. The spectra in Figs. 2(a)–2(c) originate from a $\gamma\gamma$ matrix, which was gated by a third γ ray representing one of the intense 106, 670, 1643, and 2168 keV lines in ^{38}Ar. Figure 2(a) is in coincidence with the 1900 keV and 1903 keV doublet. The 1900 keV line depopulates the level at 10 026 keV. Transitions associated with the new even-spin decay sequence 4 on the left hand side of Fig. 1 can clearly be identified, e.g., at 1055, 1451, 1524, 2135, or 3538 keV. The weak 4097 keV line at the top of band 3 cannot be seen in Fig. 2(a) due to the limited statistics and because most of the flux depopulating the levels at 11 551 and 13 685 keV proceeds via the 1375 and 2068 keV lines, which form the connection to the known negative-parity states. The 1903 keV line forms a weak connection between the previously known levels at 8974 and 7071 keV, which generates the peak at 1202 keV and a considerable fraction of the 2484 keV line in Fig. 2(a). The spectrum in Fig. 2(b) is in coincidence with the 1441 keV $11^-\rightarrow 9^-$ transition. The contribution due to the weak 1438 keV $6^+\rightarrow 4^+$ line is negligible. New transitions at, e.g., 2068, 2300, 3779, or 4097 keV are visible and could be placed unambiguously in the level scheme of Fig. 1. The lines at 1140 and 3063 keV in Fig. 2(b) seem to feed directly into the 11 617 keV 11^- state.

A number of R_{DCO} values allow for an assignment of even spins and negative parity to the 10 026, 11 551, and

TABLE I. Level energies E_x, γ-ray energies E_γ, relative intensities I_γ, angular correlation ratios R_{DCO}, and multipole assignments of transitions observed in ^{38}Ar.

E_x (keV)	E_γ (keV)	I_γ (%)	R_{DCO}	Multipolarity	I_i ($\hbar$)	I_f ($\hbar$)
2168(1)	2167.5(5)	110(3)	1.01(5)[a]	$E2$	2^{+b}	0^+
3811(1)	1642.7(4)	100(3)	0.64(3)	$E1$	3^{-b}	2^+
3937(1)	1769(1)	0.2(1)		$\Delta I=0$	2^{+b}	2^+
	3938(2)	2.1(3)		$E2$	2^+	0^+
4481(1)	669.6(2)	90(3)	0.63(3)	$E2/M1$	4^{-b}	3^-
4566(1)	2398(2)	0.7(2)		$\Delta I=0$	2^{+b}	2^+
4586(1)	105.9(1)	83(8)		$E2/M1$	5^{-b}	4^-
	775.5(3)	11(1)	1.08(7)	$E2$	5^-	3^-
5350(1)	784(1)	0.2(1)		$E2$	4^{+b}	2^+
	1413.1(4)	3.8(3)		$E2$	4^+	2^+
	1539(1)	0.9(2)		$E1$	4^+	3^-
	3183(2)	8(1)	0.98(8)[a]	$E2$	4^+	2^+
5659(1)	1073.2(4)	7.2(3)	1.08(8)	$\Delta I=0$	5^{-b}	5^-
	1178.6(6)	0.7(1)		$E2/M1$	5^-	4^-
6054(1)	703.9(3)	2.2(2)		$\Delta I=0$	4^{+c}	4^+
	1488(1)	0.4(1)		$E2$	4^+	2^+
	2116(1)	0.6(2)		$E2$	4^+	2^+
6409(1)	749.9(4)	0.3(1)		$E1$	6^{+b}	5^-
	1058(1)	1.8(2)		$E2$	6^+	4^+
	1823.3(4)	55(2)	0.56(3)	$E1$	6^+	5^-
6675(1)	2088.7(6)	5.7(6)	1.16(17)	$\Delta I=0$[c]	5^{-b}	5^-
7071(1)	2483.9(6)	10(1)	1.19(9)	$E2/M1$	6^-	5^-
	2590(1)	1.1(2)		$E2$	6^-	4^-
7289(1)	879.9(3)	1.2(1)		$\Delta I=0$	6^{+b}	6^+
	1236(1)	0.4(1)		$E2$	6^+	4^+
	1939.4(7)	7.8(6)	0.94(8)	$E2$	6^+	4^+
	2704(1)	2.6(2)		$E1$	6^+	5^-
7492(1)	1438(1)	2.4(2)	[a]	$E2$[c]	6^+	4^+
	1833(1)	0.8(2)		$E1$	6^+	5^-
	2142(1)	1.1(2)		$E2$	6^+	4^+
7509(1)	437.8(2)	0.8(1)	0.82(15)	$E2/M1$	7^-	6^-
	1100(1)	0.2(1)		$E1$	7^-	6^+
	1850(1)	0.7(3)		$E2$	7^-	5^-
	2923(1)	9.1(5)	1.14(9)[a]	$E2$	7^-	5^-
7859(1)	1184.5(4)	1.1(2)	0.59(9)	$\Delta I=1$	6	5^-
8078(1)	789.3(6)	0.5(1)		$E2/M1$	7^{+b}	6^+
	1669.4(4)	6.7(2)	1.59(12)	$E2/M1$	7^+	6^+
8126(1)	1055(1)	0.9(2)	0.83(31)[a]	$(\Delta I=0)$	$(6^-)^b$	5^-
	1451(1)	0.4(1)		$(E2/M1)$	(6^-)	5^-
	3538(2)	1.4(2)	[a]	$(E2/M1)$	(6^-)	5^-
8492(1)	1421.0(4)	3.3(4)	0.51(5)	$\Delta I=1$	6	5^-
8571(1)	492.6(2)	3.8(2)	0.61(5)	$E2/M1$	8^{+b}	7^+
	1061.4(3)	7.3(2)	0.66(7)[a]	$E1$	8^+	7^-
	1282(1)	0.3(1)		$E2$	8^+	6^+
	2162(1)	30(2)	1.01(5)[a]	$E2$	8^+	6^+
8974(1)	847.8(4)	0.4(1)		$(E2/M1)$	7^{-b}	(6^-)
	1903(1)	0.4(1)		$E2/M1$	7^-	6^-
	2300(1)	1.1(2)	1.14(23)[a]	$E2$	7^-	5^-
	2565(1)	12(1)	0.70(5)	$E1$	7^-	6^+
	3314(1)	2.5(1)	1.15(21)	$E2$	7^-	5^-
	4388(2)	4.1(2)	1.19(14)	$E2$	7^-	5^-

TABLE I. (*Continued*).

E_x (keV)	E_γ (keV)	I_γ (%)	R_{DCO}	Multipolarity	I_i ($\hbar$)	I_f ($\hbar$)
9340(1)	1848(1)	1.3(2)		$E2$	8^{+b}	6^+
	2051.3(6)	7.9(6)	1.07(11)	$E2$	8^+	6^+
	2931(1)	1.9(2)	[a]	$E2$	8^+	6^+
9350(1)	2941(2)	0.4(1)		$E1$	7^{-c}	6^+
	3691(2)	0.3(1)		$E2$	7^-	5^-
	4764(3)	0.5(1)		$E2$	7^-	5^-
9538(1)	967.4(3)	1.1(1)	0.98(10)	$\Delta I=0$	8^{+c}	8^+
	2046(1)	0.8(2)		$E2$	8^+	6^+
	2248(1)	0.8(3)		$E2$	8^+	6^+
	3128(2)	1.4(2)		$E2$	8^+	6^+
9935(1)	1364(1)	7(1)	0.46(3)[a]	$E2/M1$	9^+	8^+
10 026(1)	1900(1)	2.4(3)	1.10(34)[a]	$(E2)$	8^-	(6^-)
	1948(1)	0.9(2)		$E1$	8^-	7^+
	2517(1)	1.1(2)		$E2/M1$	8^-	7^-
	2956(2)	1.3(2)		$E2$	8^-	6^-
10 176(1)	835.3(4)	0.7(2)		$E1$	9^{-b}	8^+
	1201.8(3)	14(1)	1.09(6)	$E2$	9^-	7^-
	1605.4(4)	19(1)	0.58(3)	$E1$	9^-	8^+
10 949(1)	773(1)	0.8(3)	[a]	$\Delta I=0$	9^-	9^-
	1598(2)	0.3(1)		$E2$	9^-	7^-
	2378(1)	2.9(2)	0.83(9)[a]	$E1$	9^-	8^+
	3439(2)	0.3(1)		$E2$	9^-	7^-
11 300(1)	1364(1)	2(1)	0.46(3)[a]	$E2/M1$	10^+	9^+
	1959.5(7)	3.6(2)	1.17(21)	$E2$	10^+	8^+
11 551(1)	1374.7(4)	6.3(2)	1.29(17)	$E2/M1$	10^-	9^-
	1524.4(4)	2.6(2)	0.91(16)	$E2$	10^-	8^-
11 617(1)	1440.9(4)	21(1)	1.05(5)	$E2$	11^{-b}	9^-
11 651(2)	2301(2)	0.6(2)	1.14(23)[a]	$(E2)$	(9^-)	7^-
11 917(1)	2378(1)	0.7(2)		$E2$	10^+	8^+
	2576.2(8)	3.9(2)	0.95(16)	$E2$	10^+	8^+
11 999(2)	1050(1)	0.5(1)				$9^{(-)}$
12 108(1)	2570(2)	0.3(1)		$E2$	10^{+c}	8^+
	3537(2)	1.2(2)	[a]	$E2$	10^+	8^+
13 685(1)	2068.5(7)	3.2(2)	0.30(2)	$E2/M1$	12^-	11^-
	2134.9(6)	3.1(4)	1.18(17)	$E2$	12^-	10^-
14 121(2)	2821(2)	0.7(2)				10^+
	4185(3)	0.4(2)				9^+
14 392(1)	2285(1)	0.2(1)		$E2$	12^+	10^+
	2475.7(8)	2.4(2)	1.02(19)	$E2$	12^+	10^+
	3093(2)	0.7(2)		$E2$	12^+	10^+
14 879(2)	2962(2)	0.6(2)		$(E2)$	$(12^+)^d$	10^+
15 396(2)	3779(2)	1.6(2)	1.02(19)	$E2$	13^-	11^-
17 003(2)	2611(1)	0.9(2)	1.11(38)			
17 782(2)	4097(2)	0.5(2)				(12)
18 071(4)	3192(3)	0.4(2)		$(E2)$	$(14^+)^d$	(12^+)
21 663(5)	3592(3)	0.2(1)		$(E2)$	$(16^+)^d$	(14^+)

[a]Doublet structure.

[b]Supported by or taken from latest data evaluation.

[c]Due to or supported by stretched $E2$ connections to a state with known spin and parity [4].

[d]Assignment based on systematic rotational behavior.

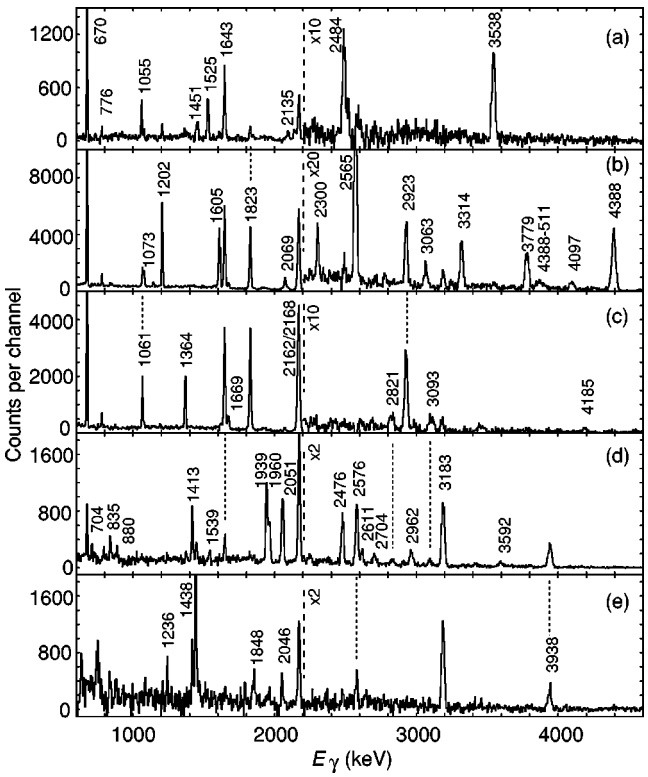

FIG. 2. Gamma-ray spectra of ^{38}Ar. They are all gated with one detected α particle, two protons, and no neutron. Panels (a), (b), and (c) are summed double-gated spectra in coincidence with (i) the 106, 670, 1643, and 2168 keV lines and (ii) the 1900/1903 keV doublet [panel (a)], the 1441 keV transition [panel (b)], and the 1364 keV doublet. Panel (d) shows the sum of spectra in double coincidence with the 1939, 2051, 2577, and 3183 keV lines in band 1. Panel (e) is measured in coincidence with the 704 keV line, which connects bands 1 and 2. Energy labels are in keV.

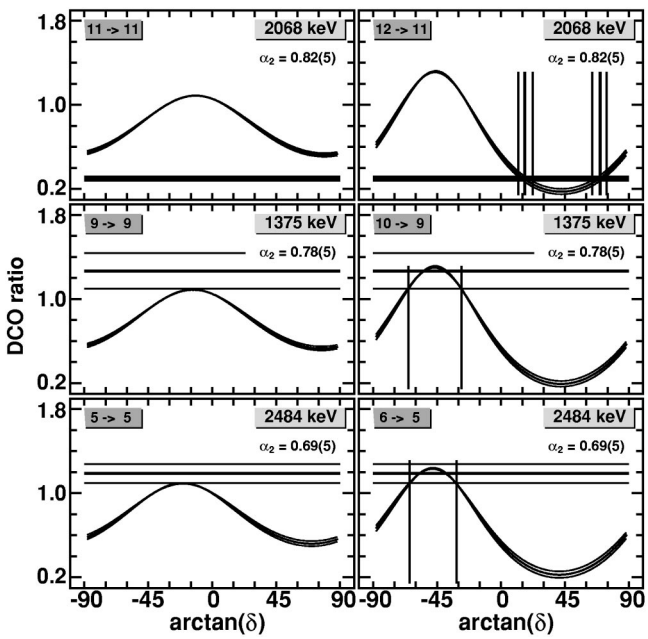

FIG. 3. The experimental DCO ratios of the 2068 (top row), 1375 (middle row), and 2484 keV (bottom row) transitions are compared to DCO ratios calculated as a function of the multipole mixing ratio δ assuming either nonstretched $\Delta I=0$ (left column) or stretched $\Delta I=1$ (right column) character by using the given alignment coefficients α_2 and detector angles according to Eq. (1).

13 685 keV levels. They also imply a modification of the spin and parity assignment of the 7071 keV state from 5^- [4] to 6^-. Figure 3 compares the measured R_{DCO} values for the 2068, 1375, and 2484 keV transitions to DCO ratios calculated as a function of the multipole mixing ratio $\delta(E2/M1)$ [or $\delta(M2/E1)$, respectively]. The results for nonstretched $\Delta I=0$ hypotheses are shown in the left column of Fig. 3, while the right column illustrates the analysis assuming stretched $\Delta I=1$ transitions. The thick and thin horizontal lines in Fig. 3 indicate the experimental R_{DCO} values and their error margins. For each panel three curves were calculated for a given alignment coefficient α_2 and its presumed upper and lower limits, respectively. The crossings of the curves with the experimental R_{DCO} values mark possible solutions for the mixing ratio δ. These are indicated by the vertical solid lines. The alignment coefficients α_2 were calculated using the relation $\alpha_2=0.55+0.02E_x$ (MeV). Including uncertainties of $\Delta\alpha_2=\pm0.05$ this assumption provides a reasonable estimate of the alignment following heavy-ion fusion evaporation reactions, provided that no long-lived isomers are encountered in the course of the decay.

The value $R_{DCO}=0.30(2)$ of the 2068 keV transition is only consistent with a stretched $\Delta I=1$ transition. The two possible solutions for the mixing ratio are $\delta_1=0.30(^{11}_{8})$ and $\delta_2=2.7(^{8}_{6})$. This fixes the spin of the 13 685 keV state to be $I=12$ and subsequently those of the 11 551 and 10 026 keV levels at $I=10$ and $I=8$, respectively. The $I=10$ assignment is also in line with the mixing-ratio analysis of the 1375 keV line shown in the middle row of Fig. 3, which yields $-2.2<\delta<-0.5$ for the $\Delta I=1$ hypothesis. The R_{DCO} values for the 1524 and 2135 keV transitions are consistent with stretched $E2$ transitions. Furthermore, a parity changing mixed $M2/E1$ character for the 2068 and 1375 keV lines can be ruled out. Using the lowest possible values of δ, their $B_W(M2)$ strengths (Weisskopf units) would outweigh the $B_W(E2)$ in-band strengths of the 2135 and 1524 keV lines by factors of more than 2 or 30, respectively. Therefore, we assign $I^\pi=8^-$, 10^-, and 12^- to the 10 026, 11 551, and 13 685 keV states. The R_{DCO} value of the 1900 keV transition in combination with the decay pattern of the 8126 keV state and previous knowledge [4] finally allows for a tentative 6^- assignment to this level.

As a result of the observation of the 2956 keV line between the 10 026 keV 8^- and 7071 keV state, the previous 5^- assignment to the latter has to be revised to 6^-, because stretched $M3$ transitions are highly unlikely to be observed in prompt in-beam γ-ray spectroscopy. This spin change is also supported by the mixing-ratio analysis of the 2484 keV line shown in the bottom row of Fig. 3, which yields $-2.0<\delta<-0.6$ for a stretched $\Delta I=1$ transition rather than $\delta\sim-0.5$ for the $\Delta I=0$ hypothesis.

The spectrum in Fig. 2(c) is in coincidence with the 1364 keV line, which is known to be a doublet from earlier studies [8]. The relevant transitions of the decay of the 8^+ yrast

level at 8571 keV can be seen at 1061, 1669, and 2162 keV, while the high-energy lines at 2821, 3093, and 4185 keV mark the connections to states of higher excitation energy and spin. The decay of the level at 14 121 keV into a 9^+ and 10^+ state hints at a spin assignment of 11^+, though it cannot be proved experimentally due to low statistics.

The spectrum in Fig. 2(d) is the sum of spectra in double coincidence with any combination of the 1939, 2051, 2576, and 3183 keV transitions and thus highlights the structures labeled 1 and 2 in Fig. 1. The 2476 keV line connects the two bands, and the 2611 keV line marks the top of band 2. Though intensively searched for, a continuation of band 2 with a 3–4 MeV transition could not be established from the present data set. The 2962 keV line, which is clearly visible in Fig. 2(d), feeds into the 11 917 keV 10^+ state. Beyond that, the situation is not clear: The 2962 keV transition is in coincidence with the 3592 keV line, but the 3192 keV line is a doublet with the 3183 keV $4^+ \rightarrow 2^+$ decay-out transition at low spin. The doublet is inferred from intensity relationships arising from the RADWARE $\gamma\gamma\gamma$ cube analysis, but both its presence and the sequence of the 3192 keV and 3592 keV transitions remain uncertain due to the limited statistics in that part of the level scheme. The strongest argument in favor of the 3192 keV line is a spectrum which is in coincidence with the 1939 keV transition at the bottom of band 1 as well as with any of the (weak) 1413, 1539, 1769, and 3938 keV transitions. This spectrum does reveal a weak line at $\sim$3192 keV, though the latter transitions run parallel to the 3183 keV line in the level scheme (cf. Fig. 1). The relative intensities of the 3192 and 3592 keV transitions (see Table I) favor the sequence shown in Fig. 1. The 1960 keV line connects band 1 to the previously mentioned 11 300 keV 10^+ state, and several other weak interband or decay-out transitions can be seen in Fig. 2(d). Some of these (1236 and 1848 keV) are highlighted in Fig. 2(e), which is a spectrum in coincidence with the 704 keV line. This transition connects the two 4^+ states in bands 1 and 2.

The 1421 keV transition, which depopulates the level at 8492 keV and which has been known from previous studies [8], has a rather large relative yield of 3.3(4)%. A total of four additional γ rays are in clear coincidence with this transition and the subsequent 2484, 106, 670, 1643, and 2168 keV lines. Their energies are 1330.1(3), 1755.8(5), 1966(1), and 2672(2) keV with relative intensities of 0.7(2)%, 0.6(2)%, 0.3(1)%, and 0.5(2)%, respectively. None of these four transitions were in mutual coincidence; i.e., they would give rise to four additional states in the level scheme with likely spins between $7\hbar$ and $8\hbar$. For the sake of clarity neither the levels nor the γ-ray transitions have been included in Fig. 1.

III. DISCUSSION

^{38}Ar has two proton holes with respect to the doubly magic core ^{40}Ca. This implies that excited states beyond spin $2\hbar$ have to involve particle-hole excitations across the spherical shell gap at particle number 20 if one neglected excitations from the $d_{5/2}$ orbit, which could create an excited 4^+ state. This state, however, is likely to lie isolated at rather high excitation energy, similar to the corresponding 9182 keV 6^+ state in ^{36}Ar [7]. Since neutrons and protons occupy the same orbits, both the energy cost of (pair-breaking) core excitations and the energy gain due to the residual interaction are of similar size for the two kinds of nucleons. In fact, the strong binding of neutron-proton two-body matrix elements favors states for which the same numbers of protons and neutrons are excited from the sd into the fp shell.

The features of the structures labeled 1, 2, 3, and 4 in Fig. 1 in ^{38}Ar are discussed in the context of large-scale shell-model (LSSM) calculations in the sd-fp model space with a filled and closed $d_{5/2}$ shell. The LSSM predictions were obtained using the diagonalization code ANTOINE [17] and an effective interaction based on that presented in Ref. [18]. Static and transitional electric moments were calculated with effective charges of $e_p = 1.5$ and $e_n = 0.5$.

Ideally, one should perform a full sd-pf calculation to describe the complete spectroscopy of ^{38}Ar. However, this is far beyond our present-day computational possibilities. Another option could be to limit the number of particles allowed to be excited from the sd shell to the pf shell to a maximum value n. The problem associated with such an approach is that it would be necessary to include up to 8p-10h configurations if one were to describe states dominated by 4p-6h components due to pairing correlations via states of 6p-8h type. This again is beyond our present-day computing possibilities. A way out of this impasse is to study fixed np-mh configurations, which excludes the mixing among different np-mh sets. However, if we deal with bands that originate from a well-defined intrinsic state, the unmixed calculations can still provide a good description, because the residual mixing should not have large effects on these structures. Hence, we have performed 2p-4h and 4p-6h calculations and located such bands. Nevertheless, we cannot aim for a perfect description because of the missing mixing. For the negative-parity states, the fixed configuration calculations do not produce any band like structure. Thus we cannot trust the unmixed calculations in that case.

Figure 4 provides the experimental (a) and calculated (b) energies relative to a rigid rotor reference. The energies were normalized to the 0_2^+ state at 3.38 MeV [4]. The predicted 2p-4h states match the spin 6-11 positive-parity sequence labeled 3 in Fig. 1. It is formed by the levels at 6409, 8078, 8571, 9935, 11 300, and (tentatively) 14 121 keV. The latter state is likely to represent the terminating 11^+ state of the 2p-4h structure. Another argument in favor of interpreting sequence 3 as being dominated by 2p-4h configurations is its connection to the negative-parity states: these positive-parity levels are mainly fed by the 3p-5h states, and they populate the low-lying 1p-3h structure.

The first, second, or third excited states of the 4p-6h calculation have been matched to the experimental ones of bands 1 and 2 based on both their excitation energies and, more importantly, on their decay patterns. The predicted and observed branching ratios are given in Table II. As a result of favoring the decay pattern rather than the excitation energy in the matching process, the predicted 10_1^+ and 10_2^+ states had to be interchanged. The observed and predicted energy curves in Fig. 4 are quite similar. The only overall difference

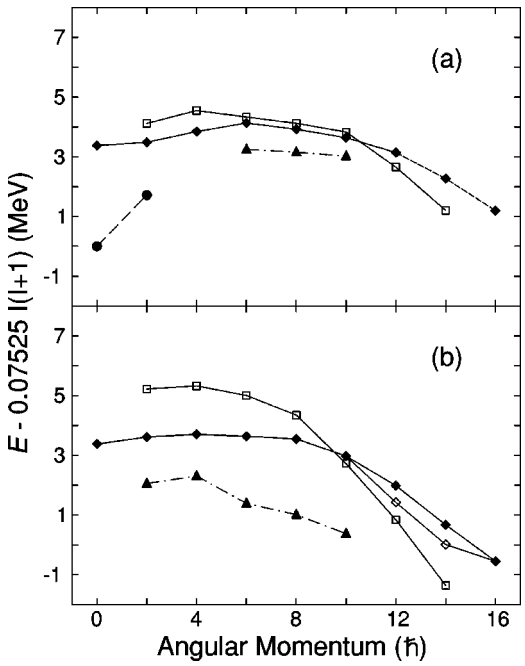

FIG. 4. Energies of positive-parity, even-spin states in ^{38}Ar. The experimentally observed (a) and calculated (b) energies are relative to a rigid rotor reference. Different symbols represent structures 1 (solid and open diamonds), 2 (open squares), and 3 (solid triangles) corresponding to the labels in Fig. 1. The solid circles are 0_1^+ and 2_1^+ states.

is that at low spins the calculated bands are much more split energetically than seen in experiment. A simple explanation for that is configuration mixing, in particular with the 2*p*-4*h* states, which are predicted to be yrast in that spin regime, while the yrast 4_1^+ state at 5350 keV is experimentally associated with band 1. A reduced relative energy between the 2*p*-4*h* and 4*p*-6*h* calculations could solve this problem and the fact that configuration mixing would increase the energy difference between the lowest and second lowest states of a given spin and parity.

The predicted and observed branching ratios are in overall good agreement. It has to be taken into account that some of the intense nonobserved branches in practice relate to very weak transitions in the experiment. For example, the predicted 29% branch for the $14_3^+ \rightarrow 12_2^+$ transition in the decay of the 18 071 keV level in band 1 would correspond to a transition with 0.1% relative intensity (cf. Table I). Table II and Figs. 4 and 5 take into account that the predicted branching ratios for the $16_1^+ \rightarrow 14_2^+ \rightarrow 12_2^+ \rightarrow 10_2^+$ and $16_1^+ \rightarrow 14_3^+ \rightarrow 12_3^+ \rightarrow 10_2^+$ sequences describe the observed top of band 1 equally well. The latter choice, however, is preferred due to the curvature in Fig. 4 and larger in-band transition rates (cf. Table II). The preference is indicated in the two corresponding figures by using solid and open symbols, respectively. The only major discrepancy in Table II is the decay of the 14 392 keV 12_1^+ state of band 2. A possible explanation lies in the closeness of both observed 10^+ and predicted 4*p*-6*h* 10^+ states. The interaction with the 2*p*-4*h* structure manifests itself experimentally from observation of the 3093, 3537, and 3128 keV transitions connecting bands 1 and 3.

TABLE II. Measured and predicted stretched $E2$ branchings b and calculated transition strengths $B(E2)$ for the 4*p*-6*h* structures in ^{38}Ar. The energies of nonobserved (n.o.) γ rays and levels have been extrapolated from the predicted energies and observed levels with the same spin and parity. Note that these energies can differ for different choices in the process of matching observed and predicted states.

E_x (keV)	$I^\pi_{i,\mathrm{th}}$ ($\hbar$)	$I^\pi_{f,\mathrm{th}}$ ($\hbar$)	E_γ (keV)	b_{expt} (%)	b_{th} (%)	$B(E2)_{\mathrm{th}}$ (e^2 fm^4)
Band 1						
5350	4_1^+	2_2^+	784	5(3)	0	0.01
		2_1^+	1413	95(3)	100	322
7289	6_1^+	4_3^+	n.o.		0	1.1
		4_2^+	1236	5(1)	0	0.2
		4_1^+	1939	95(1)	100	330
9340	8_1^+	6_3^+	n.o.		0	0.002
		6_2^+	1848	14(3)	1	7.7
		6_1^+	2051	86(3)	99	303
11 917	10_2^+	8_3^+	n.o.		0	3.4
		8_2^+	2378	15(4)	3	9.0
		8_1^+	2576	85(4)	97	223
14 879	12_3^+	10_3^+	n.o.		6	50.8
		10_2^+	2962	100	91	110
		10_1^+	n.o.		3	4.9
18 071	14_3^+	12_3^+	3192	100	70	89.4
		12_2^+	n.o.		29	25.7
		12_1^+	n.o.		2	1.0
21 663	16_1^+	14_3^+	3592	100	55	34.0
		14_2^+	n.o.		44	17.2
		14_1^+	n.o.		0	0.05
14 879	12_2^+	10_3^+	n.o.		2	13.1
		10_2^+	2962	100	95	76.7
		10_1^+	n.o.		2	2.5
18 071	14_2^+	12_3^+	n.o.		8	10.1
		12_2^+	3192	100	70	11.8
		12_1^+	n.o.		23	0.6
21 663	16_1^+	14_3^+	n.o.		44	34.0
		14_2^+	3592	100	55	17.2
		14_1^+	n.o.		1	0.05
Band 2						
6054	4_2^+	2_2^+	1488	40(13)	95	129
		2_1^+	2116	60(13)	5	1.1
7492	6_2^+	4_3^+	n.o.		0	18.7
		4_2^+	1438	69(6)	95	228
		4_1^+	2142	31(6)	5	1.6
9538	8_2^+	6_3^+	n.o.		1	3.0
		6_2^+	2046	50(15)	99	34.7
		6_1^+	2248	50(15)	1	0.2
12 108	10_1^+	8_3^+	n.o.		1	2.4
		8_2^+	2570	100	82	101
		8_1^+	n.o.		17	14.6
14 392	12_1^+	10_3^+	n.o.		1	4.7
		10_2^+	2476	92(4)	4	2.2
		10_1^+	2285	8(4)	95	80.5
17 003	14_1^+	12_3^+	n.o.		0	0.8
		12_2^+	n.o.		2	2.7
		12_1^+	2611	100	98	47.5

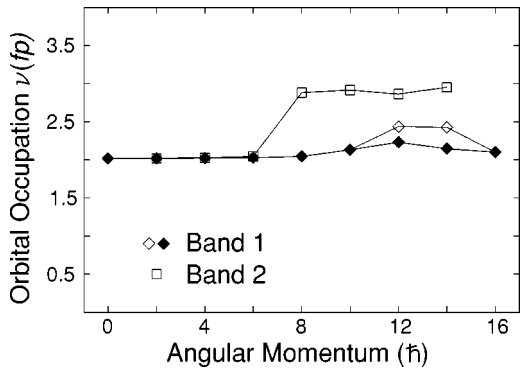

FIG. 5. Predicted summed occupancies of spherical neutron fp shells in the two lowest positive-parity deformed bands of ^{38}Ar.

Predicted neutron and proton occupation numbers of spherical j shells of the 4p-6h band 1 reveal results very similar to the prediction for the superdeformed band in ^{36}Ar [7]. Both the $f_{7/2}$ and $p_{3/2}$ orbits are active at low and intermediate spin, which gives rise to the collective behavior [16]. Towards higher spins, however, the $p_{3/2}$ shell is emptied. At the same time, the $f_{5/2}$ orbit becomes active, which leads to a decrease of collectivity towards the termination at spin $16\hbar$. This is in line with a significant reduction of predicted $B(E2)$ values, which are given in the rightmost column of Table II.

At low spin the only remarkable difference in between bands 1 and 2 is the neutron configuration in the sd shell at low and intermediate spins: While the occupation numbers are stable around two for the $s_{1/2}$ and $d_{3/2}$ in the wave function of band 1, the configuration of band 2 involves a larger fraction of the latter. Starting from spin $8\hbar$, however, the occupation numbers for band 2 look significantly different from those of band 1. First of all, the number of $p_{3/2}$ neutrons remains at a constant level of roughly one. This implies a less significant loss of collectivity towards the top of the band. In fact, the $B(E2)$ strength in this band is reduced only by a factor of 2 towards high spin, while the corresponding number in the case of band 1 is 10. Second, the summed neutron occupation of band 3 is 3, while it is around 2 for the other bands. This is illustrated in Fig. 5. Hence, the top of band 2 is based on a $\nu 3^3 \pi 3^1$ configuration rather than a more symmetric $\nu 3^2 \pi 3^2$ solution, which is proposed for band 1.

IV. SUMMARY

The high-spin excitation scheme of ^{38}Ar has been extended significantly. The excited states can be grouped according to the leading particle-hole character of their wave function. Different from the pronounced rotational bands observed in the neighboring $N=Z$ nuclei ^{36}Ar [7] and ^{40}Ca [6], the corresponding 4p-6h structure in ^{38}Ar is nonyrast over a wide spin range and competes with several different configurations. This gives rise to a considerable amount of configuration mixing within the 4p-6h bands as well as with the 2p-4h sequence at low spins. This situation is difficult to reconcile theoretically. Nevertheless, large-scale shell-model calculations provide a consistent picture for the observed level scheme. Future dedicated lifetime measurements of the 4p-6h rotational states are clearly necessary to prove their collective character. Such investigations are in progress [19].

ACKNOWLEDGMENTS

The authors thank the support from Lawrence Berkeley National Laboratory and D. Balamuth, S. Freeman, M. Leddy, and C.J. Lister for the neutron detector setup. This work was supported by the Swedish Research Council, MCyT Grant No. BFM2000-30 (A.P.), the German BMBF [06-OK-862I(0)], the Canadian NSERC, and the U.S. DOE [Grant Nos. DE-FG02-96ER40963 (UT), DE-FG05-88ER40406 (WU)]. ORNL is operated by UT-Battelle, LLC for the U.S. DOE under Contract No. DE-AC05-00OR22725.

[1] D. Rudolph *et al.*, Phys. Rev. Lett. **82**, 3763 (1999).
[2] W.J. Gerace and A.M. Green, Nucl. Phys. **A93**, 110 (1967).
[3] J.R. MacDonald, D.H. Wilkinson, and D.E. Alburger, Phys. Rev. C **3**, 219 (1971).
[4] P.M. Endt, Nucl. Phys. **A521**, 1 (1990); **A633**, 1 (1998).
[5] J.J. Simpson, S.J. Wilson, P.W. Green, J.A. Kuehner, W.R. Dixon, and R.S. Storey, Phys. Rev. Lett. **35**, 23 (1975).
[6] E. Ideguchi *et al.*, Phys. Rev. Lett. **87**, 222501 (2001).
[7] C.E. Svensson *et al.*, Phys. Rev. Lett. **85**, 2693 (2000); Phys. Rev. C **63**, 061301(R) (2001).
[8] H.J.M. Aarts, G.A.P. Engelbertink, H.H. Eggenhuisen, and L.P. Ekström, Nucl. Phys. **A321**, 515 (1979).
[9] I.-Y. Lee, Nucl. Phys. **A520**, 641c (1990).
[10] D.G. Sarantites, P.-F. Hua, M. Devlin, L.G. Sobotka, J. Elson, J.T. Hood, D.R. LaFosse, J.E. Sarantites, and M.R. Maier, Nucl. Instrum. Methods Phys. Res. A **381**, 418 (1996).
[11] M. Devlin, L.G. Sobotka, D.G. Sarantites, and D.R. LaFosse, Nucl. Instrum. Methods Phys. Res. A **383**, 506 (1996).
[12] C.E. Svensson *et al.*, Nucl. Instrum. Methods Phys. Res. A **396**, 228 (1997).
[13] D.C. Radford, Nucl. Instrum. Methods Phys. Res. A **361**, 297 (1995).
[14] J. Theuerkauf, S. Esser, S. Krink, M. Luig, N. Nicolay, O. Stuch, and H. Wolters, computer code TV, University of Cologne (unpublished).
[15] K.S. Krane, R.M. Steffen, and R.M. Wheeler, At. Data Nucl. Data Tables **11**, 351 (1973).
[16] A.P. Zuker, J. Retamosa, A. Poves, and E. Caurier, Phys. Rev. C **52**, R1741 (1995).
[17] E. Caurier, computer code ANTOINE, Strasbourg, 1989.
[18] J. Retamosa, E. Caurier, F. Nowacki, and A. Poves, Phys. Rev. C **55**, 1266 (1997).
[19] R.A.E. Austin *et al.* (unpublished).